

Energy & Environmental Science

Accepted Manuscript



This is an *Accepted Manuscript*, which has been through the Royal Society of Chemistry peer review process and has been accepted for publication.

Accepted Manuscripts are published online shortly after acceptance, before technical editing, formatting and proof reading. Using this free service, authors can make their results available to the community, in citable form, before we publish the edited article. We will replace this *Accepted Manuscript* with the edited and formatted *Advance Article* as soon as it is available.

You can find more information about *Accepted Manuscripts* in the [Information for Authors](#).

Please note that technical editing may introduce minor changes to the text and/or graphics, which may alter content. The journal's standard [Terms & Conditions](#) and the [Ethical guidelines](#) still apply. In no event shall the Royal Society of Chemistry be held responsible for any errors or omissions in this *Accepted Manuscript* or any consequences arising from the use of any information it contains.



Energy and Environmental Science

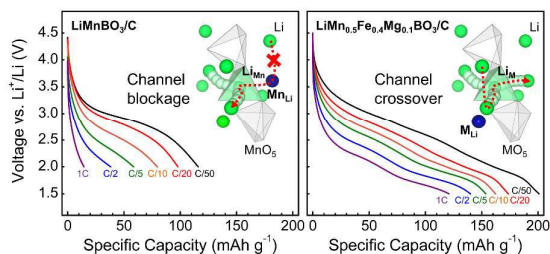
ARTICLE

Theoretical capacity achieved in a $\text{LiMn}_{0.5}\text{Fe}_{0.4}\text{Mg}_{0.1}\text{BO}_3$ cathode by using topological disorder

Jae Chul Kim,^a Dong-Hwa Seo,^a and Gerbrand Ceder^a

Graphical Abstract

Theoretical capacity and improved rate capability achieved in $\text{LiMn}_{0.5}\text{Fe}_{0.4}\text{Mg}_{0.1}\text{BO}_3$ by defect engineering to enable channel-to-channel Li migration





Theoretical capacity achieved in a $\text{LiMn}_{0.5}\text{Fe}_{0.4}\text{Mg}_{0.1}\text{BO}_3$ cathode by using topological disorder

Jae Chul Kim,^a Dong-Hwa Seo,^a and Gerbrand Ceder^a

Received 00th January 20xx,
Accepted 00th January 20xx

DOI: 10.1039/x0xx00000x

www.rsc.org/

Simple borates are attractive cathodes for lithium-ion batteries for two main reasons: covalently bonded anions offer operating stability through suppressed oxygen loss, and the borate group (BO_3) possesses the highest theoretical specific capacity for one-electron polyanion systems. In this work, we demonstrate an electrochemically superior lithium borate ($\text{LiMn}_{0.5}\text{Fe}_{0.4}\text{Mg}_{0.1}\text{BO}_3$) that delivers near theoretical capacity (98%) of 201 mAh g^{-1} at C/50, improved rate capability of 120 mAh g^{-1} at 1C, and good capacity retention. Using *ab initio* modeling, the superior Li intercalation activity is explained by both stabilization of the delithiated state and increased topological cation disorder, which counter-intuitively facilitates Li transport. Our results indicate that through engineering of defect chemistry, the basic mechanism can be modified from one-dimensional to three-dimensional conduction, thereby improving kinetics. Combined with the inherent stability of the borate group, the enhanced electrochemical properties should reinvigorate searching in the borate chemistry for new safe and high-energy cathode materials.

Introduction

The electrical energy stored as chemical energy in electrodes of Li-ion batteries has enabled our everyday life to be more efficient and effective by powering state-of-the-art smart and mobile electronics.¹⁻⁵ Yet, its technological advance, especially for emerging large-scale applications, still requires higher safety than is currently available from Li-ion cells with oxide cathode.^{4,5} Thus, designing cathode compounds that warrant safer operation without compromising the energy density remains an ongoing challenge to battery scientists and engineers.^{4,5}

Materials with a polyanionic framework are advantageous as covalently bonded anions provide definite stability against oxygen loss during charging.⁶⁻⁸ However, a critical obstacle for their successful application lies in the low charge to mass/volume ratio of the polyanion that often leads to lower achievable capacity than for oxides. Simple borates (BO_3) may give a reasonable capacity/safety tradeoff as it is one of the lightest polyanions, leading to the highest theoretical capacity among the polyanionic cathodes assuming a one-electron reaction.^{9,10} In particular, lithium manganese borate (LiMnBO_3) has generated growing interests due to the high theoretical capacity of 222 mAh g^{-1} .¹⁰⁻¹⁵

However, the electrochemical performance of LiMnBO_3 needs major improvement to become a practical cathode

material.¹⁰⁻¹⁵ The hexagonal polymorph of LiMnBO_3 does not exhibit meaningful Li intercalation capacity unless its particle size is carefully controlled below 20 nm and intensive carbon coating is applied.^{10,15,16} This kinetic limitation of the hexagonal compound is consistent with the high activation barriers predicted for Li hopping of 723 meV in this structure.¹¹ The electrochemical properties of monoclinic LiMnBO_3 depend on synthesis conditions and carbon additives, but half of the theoretical capacity remains unachievable at C/20 or higher rates within a reasonable voltage window.¹¹⁻¹⁴

A reasonable strategy to improve the performance of monoclinic LiMnBO_3 is to substitute Mn by some Fe and Mg: LiFeBO_3 and LiMgBO_3 exist in the monoclinic form,^{10,17} making substitution likely.^{18,19} Many Fe^{2+} -based polyanionic cathodes tend to outperform their Mn^{2+} -counterparts in terms of capacity, rate capability, and cyclability.¹⁹⁻²⁶ Moreover, in our previous work, we found that Mg substitution enhances the capacity retention of LiMnBO_3 and largely stabilizes the delithiated structure.²⁷

In this paper, we report and analyze the effect of partial Fe and Mg substitution on the electrochemical properties of monoclinic LiMnBO_3 by a computational and experimental investigation. We target the composition of $\text{LiMn}_{0.5}\text{Fe}_{0.4}\text{Mg}_{0.1}\text{BO}_3$ with theoretical capacity of 205 mAh g^{-1} . Although Fe substitution can help to increase the achievable capacity, it lowers the average potential as shown in Supplementary Information, **Figure S1**, and reported in the literature.^{19,28,29} While Mg incorporation stabilizes the structure,²⁷ its content needs to be limited so as not to compromise theoretical capacity too much. As investigated previously,²⁷ 10% Mg substitution is chosen as a reasonable trade-off between cyclability and achievable capacity. As we

^a Department of Materials Science and Engineering, Massachusetts Institute of Technology, Cambridge, MA 02139, USA.

Corresponding author's Email: gceder@mit.edu

Electronic Supplementary Information (ESI) available: See

DOI: 10.1039/x0xx00000x

present results related to monoclinic $\text{LiMn}_{0.5}\text{Fe}_{0.4}\text{Mg}_{0.1}\text{BO}_3$ only, the compound will hereafter be noted without indicating its crystal structure.

2. Methods

Computation. In our computational study, the designated $\text{LiMn}_{0.5}\text{Fe}_{0.4}\text{Mg}_{0.1}\text{BO}_3$ composition is approximated by $\text{LiMn}_{0.5}\text{Fe}_{0.375}\text{Mg}_{0.125}\text{BO}_3$ with a $2a \times b \times c$ supercell. *Ab initio* calculations on $\text{Li}_{1-x}\text{Mn}_{0.5}\text{Fe}_{0.375}\text{Mg}_{0.125}\text{BO}_3$ ($x = 0, 0.375, 0.625,$ and 0.875) were performed using density functional theory (DFT) in the generalized gradient approximation with Hubbard U corrections (GGA + U, $U = 3.9$ eV for Mn and 4.0 eV for Fe).³⁰ All computations were performed with plane-augmented wave pseudopotentials, as implemented in the Vienna *Ab initio* Simulation Package.^{31, 32}

Total energies for $\text{LiMn}_{0.5}\text{Fe}_{0.375}\text{Mg}_{0.125}\text{BO}_3$ were computed by substituting 3/8 and 1/8 of Mn with Fe and Mg, respectively, in the monoclinic LiMnBO_3 supercell referenced in the inorganic crystal structure database (ICSD, No. 200535).^{33, 34} A large number of structural orderings were created by using the enumeration technique reported by Hart *et al.*³⁵ and the 100 Mn/Fe/Mg arrangements with the lowest electrostatic energy were calculated with DFT.³⁶ The same enumeration and electrostatic ranking approach³⁷ was used to generate Li/Vacancy ordering in the cell with the lowest energy cation configuration. Thirty Li/Vacancy arrangements were calculated with DFT at each composition, $x = 0.375, 0.625,$ and 0.875 in $\text{Li}_{1-x}\text{Mn}_{0.5}\text{Fe}_{0.375}\text{Mg}_{0.125}\text{BO}_3$.

The Li migration barrier in $\text{LiMn}_{0.5}\text{Fe}_{0.375}\text{Mg}_{0.125}\text{BO}_3$ was calculated by the nudged elastic band (NEB) method.³⁸ To avoid the charge ordering issue in GGA + U, standard GGA was employed to compute the elastic band on supercells containing a single vacancy out of 16 Li sites. The lattice parameters were constrained at the optimized GGA + U values of $\text{LiMn}_{0.5}\text{Fe}_{0.375}\text{Mg}_{0.125}\text{BO}_3$.

Experimental procedure. To produce the $\text{LiMn}_{0.5}\text{Fe}_{0.4}\text{Mg}_{0.1}\text{BO}_3$ compound, a stoichiometric batch of Li_2CO_3 (Alfa Aesar, 99.99%), $\text{MnC}_2\text{O}_4 \cdot 2\text{H}_2\text{O}$ (Alfa Aesar, 99.995%), $\text{FeC}_2\text{O}_4 \cdot 2\text{H}_2\text{O}$ (Alfa Aesar, 99.999%), $\text{MgC}_2\text{O}_4 \cdot 2\text{H}_2\text{O}$ (Alfa Aesar, 99.9%), and H_3BO_3 (Alfa Aesar, 99.8%) were dispersed into $\text{C}_3\text{H}_6\text{O}$ (Sigma Aldrich, 99%) and ballmilled at 300 rpm for 72 h. The mixed precursor was completely dried and then calcined at 350°C for 10 h under flowing argon. After intermediate grinding, the powder specimen was formed into a disc-shaped pellet and isostatically pressed in a cold oil bath by 55 MPa to ensure homogeneous and firm contact between powders. The green-body was fired at 550°C for 10 h under argon atmosphere, resulting in the target phase. To carbon coat the $\text{LiMn}_{0.5}\text{Fe}_{0.4}\text{Mg}_{0.1}\text{BO}_3$ powder, 10 wt% sucrose (EMD, 99%) were blended and ground by planetary ballmilling at 350 rpm for 5 h and annealed at 525°C for 20 h under argon atmosphere. High resolution transmission electron microscopy (HRTEM) in **Figure S2** confirms formation of the coating (3–4 nm thick).

X-ray diffraction (XRD) and scanning electron microscopy (SEM) were performed to investigate the crystal structure, and particle size distribution, respectively. The X-ray diffraction patterns were collected on a Rigaku RU300 diffractometer using

Cu-K_α radiation, and Rietveld refinement of the powder diffraction data was performed with X'pert HighScorePlus software. SEM images were taken in a Helios Nanolab 600 and processed by the ImageJ software to extract information about particle size distribution.³⁹

Battery cathodes were fabricated with 80 wt% active material, 15 wt% carbon black (Timcal, Super P), and 5 wt% polytetrafluoroethylene (PTFE) (Dupont, Teflon 8A). The active material was blended with carbon black by planetary ballmilling for 30 min and then mixed manually with PTFE in an argon-filled glovebox. A customized Swagelok cell was assembled inside the glovebox with a Li metal foil anode, polymer separator, and carbon-coated $\text{LiMn}_{0.5}\text{Fe}_{0.4}\text{Mg}_{0.1}\text{BO}_3$ ($\text{LiMn}_{0.5}\text{Fe}_{0.4}\text{Mg}_{0.1}\text{BO}_3/\text{C}$) cathode film (200 μm -thick and 7.94 mm in diameter) soaked in 1 M of LiPF_6 in ethylene carbonate (EC):dimethyl carbonate (DMC) (1:1 by volume) electrolyte. The cell was tested on Maccor 2200 and Solartron 1470E at RT. The loading density of the cathode was approximately 2.5 mg cm^{-2} , and the cell was cycled galvanostatically at different C-rates ($1 \text{ C} = 205 \text{ mA g}^{-1}$) within 4.5 – 1.5 V. The (discharge) rate capability was estimated by charging at a C/50 rate, holding at 4.5 V, and discharging to 1.5 V at various C-rates ranging from C/50 to 1C.

In situ XRD patterns were collected on Bruker D8-Advance Da Vinci diffractometer using Mo-K_α ($\lambda = 0.71074 \text{ \AA}$) radiation for $\text{LiMn}_{0.5}\text{Fe}_{0.4}\text{Mg}_{0.1}\text{BO}_3/\text{C}$. The cathode was galvanostatically charged and discharged at a C/80 rate on a Solartron SI 1287 tester. During the electrochemical cycle, 39 scanning jobs were periodically performed from 8.5° to 19.5° 2-theta with a 0.01° resolution. Prior to the *in situ* experiment, the cell was cycled once within 4.5 – 1.5 V galvanostatically at a C/20 rate, held at 1.5 V for 1 h, and relaxed for 10 h to ensure a fully discharged state.

Results

Computation. *Ab initio* computation predicts that Fe and Mg will form a solid solution with Mn at the synthesis temperature of 550°C (Supplementary Information). **Figures 1a** and **b** show the unit cells of the most stable lithiated configurations ($\text{Li} = 1$) and its delithiated form ($\text{Li} = 0.125$). However, given the very small positive formation energies of the Mn/Fe/Mg ordered states (**Figure S3**), it is likely that at the synthesis temperature of 550°C the cation arrangement will be disordered. By removing Li from the lattice, the *a*-axis expands from 5.221 to 5.535 \AA , the *b*-axis remains almost unchanged at around 9.00 \AA , but the *c*-axis contracts from 10.433 to 9.938 \AA . A potential Li diffusion path in **Figure 1c**, visualized by the bond valence sum (BVS) method, indicates one-dimensional (1-D) transport along the *c*-axis through the $\text{LiMn}_{0.5}\text{Fe}_{0.375}\text{Mg}_{0.125}\text{BO}_3$ framework. This Li pathway is identical to that of LiMnBO_3 and LiFeBO_3 in the ordered states.^{9, 26} The migration barrier of Li in $\text{LiMn}_{0.5}\text{Fe}_{0.375}\text{Mg}_{0.125}\text{BO}_3$ depends on local arrangement of Mn, Fe, and Mg around the pathway, as shown in **Figures 1d-g**. The highest calculated barrier is 530 meV when Li migrates from the site marked by a red triangle in Figure 1d to the site in Figure 1e along *c*-axis. This value is comparable to LiMnBO_3 (491–509 meV) but higher than in LiFeBO_3 (437 meV).^{11, 28}

Table 1 summarizes the relative energies (ΔE) of $\text{Li}_{1-x}\text{Mn}_{0.5}\text{Fe}_{0.375}\text{Mg}_{0.125}\text{BO}_3$ ($0 \leq x \leq 0.875$) with respect to the ground states generated by the convex-hull construction.⁴⁰ The energy value scales with instability, indicating how energetically far the given phase is from the ground states. Increasing ΔE values with respect to x suggest that the structure destabilizes upon Li removal. Even so, the values for $\text{Li}_{1-x}\text{Mn}_{0.5}\text{Fe}_{0.375}\text{Mg}_{0.125}\text{BO}_3$ are distinguishably smaller than those for $\text{Li}_{1-x}\text{MnBO}_3$ at the same Li contents.²⁷ Ground states for each composition of $\text{Li}_{1-x}\text{Mn}_{0.5}\text{Fe}_{0.375}\text{Mg}_{0.125}\text{BO}_3$ are listed in the Supplementary Information, **Table S1**.

Table 1. The calculated unit cell parameters and relative energies (ΔE) of the most stable configurations of $\text{Li}_{1-x}\text{Mn}_{0.5}\text{Fe}_{0.375}\text{Mg}_{0.125}\text{BO}_3$ ($x = 0, 0.375, 0.625, \text{ and } 0.875$). For reference, The ΔE values of $\text{Li}_{1-x}\text{MnBO}_3$ and $\text{Li}_{1-x}\text{FeBO}_3$ ($x = 0, 0.375, 0.625, 0.875, 1$)²⁷ are also listed.

x	$\text{Li}_{1-x}\text{MBO}_3$		
	$\text{M} = \text{Mn}_{0.5}\text{Fe}_{0.375}\text{Mg}_{0.125}$	$\text{M} = \text{Mn}$ ²⁷	$\text{M} = \text{Fe}$ ²⁷
	ΔE (meV)	ΔE (meV)	ΔE (meV)
0	1.5	4	0
0.375	48.6	60	35
0.625	91.1	107	58
0.875	113.3	130*	59
1	N/A	140	54

*The value is interpolated.

Formation of solid solution. **Figure 2a** shows the XRD pattern and Rietveld-refined profile obtained from the as-synthesized $\text{LiMn}_{0.5}\text{Fe}_{0.4}\text{Mg}_{0.1}\text{BO}_3$ powder. All major peaks for the monoclinic structure are indexed, indicating that both Fe and Mg have incorporated into the LiMnBO_3 host phase. The lattice parameters ($a = 5.169 \text{ \AA}$, $b = 8.899 \text{ \AA}$, and $c = 10.2277 \text{ \AA}$) also suggests formation of a complete solid solution as they are in good agreement with the expected lattice parameters that can be estimated from those of LiMnBO_3 , LiFeBO_3 , and LiMgBO_3 by Vegard's rule, as well as with the computed ones ($a = 5.211 \text{ \AA}$, $b = 9.00 \text{ \AA}$, and $c = 10.433 \text{ \AA}$).^{10, 11, 17, 41} Given the overestimation of lattice constants with GGA + U, the small difference between calculated and experimental lattice parameters is to be expected. Peaks for $\text{Mn}_3(\text{BO}_3)_2$ are observed, but its amount is estimated to be about 0.4%. Elemental analysis obtained from direct current plasma emission spectroscopy in **Table S2** confirms the target stoichiometry, leading us to conclude that Fe and Mg substitute a portion of Mn in the monoclinic host, and a highly pure $\text{LiMn}_{0.5}\text{Fe}_{0.4}\text{Mg}_{0.1}\text{BO}_3$ compound is obtained.

Compounds synthesized by a solid-state method tend to have a fair amount of disorder.^{28, 42} The local polyhedral environments of Li and transition metal (**M**) have similar coordination number and size,^{10, 11, 43} making disorder between Li and **M** likely. We refer to these antisites as Li_M for Li in the transition metal site and M_Li for transition metal in the Li site. Refining the XRD pattern with partial Mn, Fe, and Mg occupancies in Li the sites leads to 2% Mn_Li and 9.6% Fe_Li (and therefore 2% Li_Mn and 9.6% Li_Fe). The Mg_Li occupancy cannot be refined. It should be emphasized that the simulated pattern based on a structural model without the antisite occupancies does not fit to the

observed one, showing substantial peak intensity mismatch, as shown in **Figure S4**. The detailed refinement procedure is described in the Supplementary Information, and the results are summarized in **Table S3**.

Particle morphology and size distribution. **Figure 2b** shows the morphology of the $\text{LiMn}_{0.5}\text{Fe}_{0.4}\text{Mg}_{0.1}\text{BO}_3/\text{C}$ particles as observed with SEM. The material forms well-defined primary particles ranging in size from 50 to 250 nm. **Figure 2c** plots the particle size distribution of $\text{LiMn}_{0.5}\text{Fe}_{0.4}\text{Mg}_{0.1}\text{BO}_3/\text{C}$ as measured from the SEM. Fitting to a Gaussian distribution suggests that the mean particle size is 106 nm.

Formation of antisite disorder. We calculate the antisite energy in the Fe and Mg substituted LiMnBO_3 structure to give further support to the formation of $\text{Li}_\text{M} - \text{M}_\text{Li}$ pairs. From the most stable configuration of $\text{LiMn}_{0.5}\text{Fe}_{0.375}\text{Mg}_{0.125}\text{BO}_3$, 1/16 of Li in the supercell was exchanged with the surrounding Mn, Fe, and Mg, one at a time, to obtain formation energies of $\text{Li}_\text{Mn} - \text{Mn}_\text{Li}$, $\text{Li}_\text{Fe} - \text{Fe}_\text{Li}$, and $\text{Li}_\text{Mg} - \text{Mg}_\text{Li}$ antisite pairs, respectively. We define the smallest total energy difference between $\text{LiMn}_{0.5}\text{Fe}_{0.375}\text{Mg}_{0.125}\text{BO}_3$ with and without the antisite pair as the antisite formation energy.

Figures 3a-g shows the calculated antisite formation energies of $\text{LiMn}_{0.5}\text{Fe}_{0.375}\text{Mg}_{0.125}\text{BO}_3$. **Figure 3a** gives the antisite energy in LiMnBO_3 for comparison. Each square, circle, and triangle represents the antisite energy when **M** switches its position with the nearest, the second nearest, and the third nearest Li, respectively. The antisite formation energy varies with the distance between the Li_M and M_Li and is the lowest when the $\text{Li} - \text{M}$ distance is the smallest. By comparing with the antisite energies of $\text{Li}_\text{Mn} - \text{Mn}_\text{Li}$ pair in LiMnBO_3 in **Figure 3a**,²⁸ it is clear that partial Fe and Mg substitution of Mn lowers the $\text{Li}_\text{M} - \text{M}_\text{Li}$ antisite energy and will induce more antisite disorder in the structure than in the unsubstituted end member. The lowest antisite energy at 1/16 concentration is 464 meV for the $\text{Li}_\text{Fe} - \text{Fe}_\text{Li}$ pair in **Figure 3c**. However, it should be emphasized that the second and third lowest antisite energies of the $\text{Li}_\text{Fe} - \text{Fe}_\text{Li}$ pair are 493 and 508 meV, which are in a similar scale with the lowest energy.

Fixing the lowest energy antisite pair in the structure, the same calculation is performed at an antisite concentration of 1/8 (*i.e.*, 1/16 $\text{Li}_\text{Fe} - \text{Fe}_\text{Li}$ + 1/16 $\text{Li}_\text{M} - \text{M}_\text{Li}$) to investigate the preferred geometrical relation of antisites, and the results are shown in **Figure 3e-g**. This concentration is close to the experimentally obtained total antisite occupancies (11.6%). The lowest energy antisite configuration at 1/8 concentration is 856 meV for two $\text{Li}_\text{Fe} - \text{Fe}_\text{Li}$ pairs. Note that formation of the other $\text{Li}_\text{Fe} - \text{Fe}_\text{Li}$ + $\text{Li}_\text{M} - \text{M}_\text{Li}$ pairs also have similar energies to the lowest one. The results imply that many of the possible antisite configurations can occur with almost equal preference throughout the $\text{LiMn}_{0.5}\text{Fe}_{0.375}\text{Mg}_{0.125}\text{BO}_3$ lattice at elevated temperatures.

Electrochemical performance. **Figure 4a** shows the second charge and discharge curves for $\text{LiMn}_{0.5}\text{Fe}_{0.4}\text{Mg}_{0.1}\text{BO}_3/\text{C}$ at two different rates. Voltage profiles of the first three cycles for each rate are shown in **Figure S5**. A capacity of 192 mAh g^{-1} is achieved at both charge and discharge at a C/50 rate. The

plateau-like features at 3.7 V and 3 V in charging and 2.9 V and 2.3 V in discharging can be respectively assigned to the reversible $\text{Mn}^{2+}/\text{Mn}^{3+}$ and $\text{Fe}^{2+}/\text{Fe}^{3+}$ redox reactions^{9, 11} with the corresponding capacities of 113 and 79 mAh g^{-1} in charging and 117 and 75 mAh g^{-1} in discharging. The capacity at C/20 cycling is 169 mAh g^{-1} . From observing the charge profile, the capacity reduction from the rate increase is mainly due to charging above 3.7 V. Note that the voltage profiles in Figure 4a show an additional feature at ~2 V. Bo *et al.* discussed that the $\text{Fe}^{2+}/\text{Fe}^{3+}$ redox couple when in the Li sites (*i.e.*, Fe_{Li}) is responsible for the 2 V reaction.⁴⁴ Since $\text{LiMn}_{0.5}\text{Fe}_{0.4}\text{Mg}_{0.1}\text{BO}_3$ in this study includes an amount of Fe_{Li} antisites (9.6%), as estimated by Rietveld refinement in Figure 2a, the low voltage intercalation may be related to the Fe redox reaction in the Li sites.

The results obtained with $\text{LiMn}_{0.5}\text{Fe}_{0.4}\text{Mg}_{0.1}\text{BO}_3/\text{C}$ are in stark contrast to the capacity of LiMnBO_3/C obtained at a C/20 rate as shown in Figure 4a and in the literature¹¹⁻¹⁴. Given that generally achievable capacities in LiMnBO_3/C range from 80 to 120 mAh g^{-1} with similar $\text{Mn}^{2+}/\text{Mn}^{3+}$ redox potentials at comparable rates, a large portion of the inactive $\text{Mn}^{2+}/\text{Mn}^{3+}$ reaction is effectively replaced by the active $\text{Fe}^{2+}/\text{Fe}^{3+}$ reaction, leading to significant charge and discharge capacities in our mixed compound. Moreover, it should be emphasized that the voltage profile of LiMnBO_3/C exhibits a leveling-off below 1.8 V and the associated discharge capacity surpasses the charge one. This implies a conversion-type reaction in LiMnBO_3/C , which does not occur in $\text{LiMn}_{0.5}\text{Fe}_{0.4}\text{Mg}_{0.1}\text{BO}_3/\text{C}$.

The capacity retention of $\text{LiMn}_{0.5}\text{Fe}_{0.4}\text{Mg}_{0.1}\text{BO}_3/\text{C}$ corresponding to the C/20 rate is plotted in Figure 4b. Note that the charge capacity in the first cycle is smaller than that of following discharge (also shown in Figure S5), which can be related to oxidation of Fe^{2+} at the surface in the pristine powder, as similarly observed in LiFeBO_3 cathodes.^{9, 45} This phenomenon disappears in the subsequent cycles, and the cell operates in a reversible manner. Unlike the plain LiMnBO_3 case,²⁷ discoloration of the Li anode due to Mn deposition after cycling was not observed with the $\text{LiMn}_{0.5}\text{Fe}_{0.4}\text{Mg}_{0.1}\text{BO}_3/\text{C}$ cathode, implying that Mg substitution minimizes Mn dissolution, as already demonstrated in our previous study.²⁵ The average measured on the discharge capacity fading rate is 1.6% per cycle for 20 cycles at a C/20 rate.

Figures 4c and d show discharge curves of LiMnBO_3/C and $\text{LiMn}_{0.5}\text{Fe}_{0.4}\text{Mg}_{0.1}\text{BO}_3/\text{C}$ at RT for different discharge rates. The obtained discharge energy density and specific power for LiMnBO_3/C and $\text{LiMn}_{0.5}\text{Fe}_{0.4}\text{Mg}_{0.1}\text{BO}_3/\text{C}$ are also plotted in the inset of Figure 4c and d. Note that we use 1.5 V voltage cutoff for $\text{LiMn}_{0.5}\text{Fe}_{0.4}\text{Mg}_{0.1}\text{BO}_3/\text{C}$ to fully activate the all $\text{Fe}^{2+/3+}$ redox reaction while 2.0 V for LiMnBO_3/C to avoid a conversion-type reaction, as discussed in Supplementary Information (Figure S6). Charged by a constant current (C/50) followed by constant voltage (4.5 V for 2 h) (CCCV-mode), the discharge capacity of LiMnBO_3/C cathode at C/50 is 120 mAh g^{-1} . However, at higher rates, the capacity drops rapidly, and only 19 mAh g^{-1} is achieved at a 1C rate. In contrast, partial Fe and Mg substitution significantly improves the rate capability: the $\text{LiMn}_{0.5}\text{Fe}_{0.4}\text{Mg}_{0.1}\text{BO}_3/\text{C}$ cathode at C/50 reaches 201 mAh g^{-1} , which is 98% of the theoretical value. To the best of our knowledge, this is the largest discharge capacity reported in the monoclinic borate system at RT. Although the obtained capacity

decreases as the rate increases, the $\text{LiMn}_{0.5}\text{Fe}_{0.4}\text{Mg}_{0.1}\text{BO}_3/\text{C}$ cathode maintains respectable rate capability. At a 1C rate, it is still capable of delivering 120 mAh g^{-1} .

In situ XRD. The structural evolution of $\text{LiMn}_{0.5}\text{Fe}_{0.4}\text{Mg}_{0.1}\text{BO}_3/\text{C}$ upon Li extraction and insertion was analyzed with *in situ* XRD. As shown in the full patterns in Figure 5a, the monoclinic structure does not undergo any major phase decomposition or conversion during charging (192 mAh g^{-1}) or discharging (180 mAh g^{-1}) within a 4.5 – 1.5 V window. Rather, the topmost position of a peak that lumps together the reflections of (200), (130), and (004), shown in Figure 5b, shifts to the higher angle upon charging, which is a typical indication of Li deintercalation in the LiMBO_3 system.^{9, 11, 41} The diffraction peak reverts to its original position upon lithiation. In addition, the width of the peak in Figure 5b broadens while the intensity decreases upon charging. This shape change is also recovered in the discharging process. Therefore, the result of *in-situ* XRD provides strong evidence that Li intercalation in $\text{LiMn}_{0.5}\text{Fe}_{0.4}\text{Mg}_{0.1}\text{BO}_3/\text{C}$ occurs topotactically and reversibly.

Discussion

Effects of substitution on phase stability. We investigate which factors may be contributing to the improved performance of the Fe and Mg substituted borates. Table 1 shows that the substituted composition has a lower driving force for decomposition as compared to LiMnBO_3 , indicating improved stability upon delithiation. We consider that the superior stability of Fe^{3+} in trigonal bipyramidal sites and the presence of electrochemically inert Mg in the framework likely help to stabilize the delithiated structure.²⁷ A substantial amount of conversion-type reaction is often involved in the discharge process below 1.8 V for LiMnBO_3 and LiFeBO_3 .^{13, 41, 45} However, our voltage-capacity profiles in Figure 4a and *in situ* XRD results in Figure 5 give no indication of such a conversion reaction for $\text{LiMn}_{0.5}\text{Fe}_{0.4}\text{Mg}_{0.1}\text{BO}_3/\text{C}$, implying that Mg substitution contributes to the enhanced stability in the 4.5 – 1.5 V window.

Effects of substitution on Li migration. According to computational results shown in Figure S7 and reported in the literature,²⁸ LiMnBO_3 can be regarded as an electronic insulator due to a large bandgap (3.15 eV – computed), which may be responsible for poor rate capability. However, given that the calculated bandgap of $\text{LiMn}_{0.5}\text{Fe}_{0.375}\text{Mg}_{0.125}\text{BO}_3$ (3.05 eV) is similar to that of LiMnBO_3 , differences in electronic structure between the two materials are small and not likely to be the reason for the improved electrochemical performance.

Fe and Mg substitution do not alter the fundamental diffusion characteristics of LiMnBO_3 such as the 1-D pathway and the average migration barrier of ~500 meV since they are largely controlled by the cation and anion topology of the monoclinic framework. However, the substitution induces a significant amount of antisite disorder, 11.6% as estimated by Rietveld refinement and supported by *ab initio* computation. Typically, M_{Li} antisites can impede 1-D Li diffusion by blocking its pathway, leading to substantial degradation of Li intercalation capacity, especially when the particle size is larger than 100 nm.⁴⁰ The presence of $\text{Li}_{\text{Mn}} - \text{Mn}_{\text{Li}}$ disorder has been used to

rationalize the limited capacity of LiMnBO_3/C .⁴⁶ In the context, the improved electrochemical performance of $\text{LiMn}_{0.5}\text{Fe}_{0.4}\text{Mg}_{0.1}\text{BO}_3/\text{C}$ is surprising given the very significant antisite concentration, which is twice as large as in LiMnBO_3/C .⁴⁶ This contradicts the intuitive expectation for 1-D diffusion, and leads us to conclude that the Li transport mechanism in Fe and Mg substituted LiMnBO_3 may be different from the unsubstituted LiMnBO_3 .

Geometrical configuration of antisite disorder. To understand why almost theoretical capacity can be achieved in $\text{LiMn}_{0.5}\text{Fe}_{0.4}\text{Mg}_{0.1}\text{BO}_3/\text{C}$, we analyze how the antisite configuration and concentration affects the overall performance. **Figures 6a** and **b** depict the Li trajectory nearby the $\text{Li}_M - \text{M}_{Li}$ pair in two distinct arrangements. The actual trajectories are obtained from the NEB calculation, but visualized by the BVS method. Figure 6a corresponds to the second lowest and 6b to the lowest energy configurations. For comparison, the antisite-free configuration is shown in **Figure 6c**. In Figure 6a, the M_{Li} antisite blocks a 1-D channel. Although the Li_M antisite facilitates crossover between different Li channels, Li in the blocked channel cannot crossover through Li_M as M_{Li} directly sits in the crossover pathway: instead, Li_M connects two unblocked channels. As a result, M_{Li} locally blocks this Li diffusion, impeding further intercalation.

M_{Li} in the lowest energy antisite configuration shown in Figure 6b also blocks a 1-D channel. However, it may not trap Li in the channel but forward it to the neighboring channels as the associated Li_M in this defect configuration provides a bridging site for crossover into other channels. **Figure 7a** displays detailed possible crossover paths and their activation barriers for this $\text{Li}_{Mn} - \text{Mn}_{Li}$ configuration. Depending on the particular detour taken, the crossover can have migration barrier of 268 (green-blue, path 0-6-12^L) or 634 (green-red, path 0-6-12^H) meV. The crossover for the equivalent $\text{Li}_{Fe} - \text{Fe}_{Li}$ configuration in **Figure 7b** follows almost identical paths due to the geometrical similarity of cation arrangement but has different 540 (green-blue, path 0-6-12^L) and 658 meV (green-red, path 0-6-12^H) barriers due to different surrounding cations. For $\text{Li}_{Mg} - \text{Mg}_{Li}$ configuration shown in **Figure 7c**, the activation barriers are 560 (green-red, path 0-6-12^H) and 313 meV (green-blue, path 0-6-12^L). Note that lower barrier crossover through Li_{Mg} occurs in a different direction from the Li_{Mn} and Li_{Fe} . In all cases, Li can rather easily crossover from the blocked channel via the lower barrier path and continue 1-D migration in the unblocked channel. Therefore, this particular antisite configuration, regardless of the kind of cation, **M**, can redirect Li migration, and therefore does not limit capacity.

Overall concentration of antisite disorder. Since the lowest and the other antisite configurations shown in Figures 3b-g are energetically very close, it is likely that various antisite configurations occur in the actually synthesized $\text{LiMn}_{0.5}\text{Fe}_{0.4}\text{Mg}_{0.1}\text{BO}_3$ compound. As the configuration and distribution of the antisite pairs become random, the Li-trapping (second lowest energy) and Li-redirecting (lowest energy) antisites should both exist. Assuming a dilute antisite concentration, the disorder will deteriorate Li mobility in LiMBO_3 compared to the antisite-free case due to the isolated Li-

trapping antisites shown in Figure 6a. The diffusion limitation in LiMnBO_3 can be understood as caused by this dilute antisite concentration (~5.5%).⁴⁶

In contrast, when a substantial amount of antisites is present, the low barrier paths in Figures 6b and 7 can percolate, which enables the channel-to-channel crossover to become the dominant diffusion mechanism. This allows facile Li transport that can bypass the 1-D transport along the *c*-axis, making the material essentially a three-dimensional (3-D) diffuser. A Total of 11.6% disorder in $\text{LiMn}_{0.5}\text{Fe}_{0.4}\text{Mg}_{0.1}\text{BO}_3/\text{C}$ may be enough to form a 3-D percolating low barrier path, similar to what has been demonstrated in the disordered rocksalt $\text{Li}_2\text{MoO}_3\text{-LiCrO}_2$ system and $\text{Li}_x\text{V}_2\text{O}_5$ cathode.^{47, 48} Hence, the large Li activity in $\text{LiMn}_{0.5}\text{Fe}_{0.4}\text{Mg}_{0.1}\text{BO}_3$ can be understood in relation to the topological effect of the substitution in edge-sharing MnO_5 chains and the resulting antisite disorder, which enables feasible Li transport. This is a refreshing perspective on how the concentration of antisite disorder affects the 1-D Li intercalation. Counter to intuition, channel blockage by the antisites is not always detrimental in 1-D materials if low-barrier crossover pathways between the channels can percolate. Thus, our model may provide hints to enhance the electrochemical performance of other LiMBO_3 cathodes, such as LiCoBO_3 ,⁴⁹⁻⁵¹ which have similar 1-D Li diffusion and suffer from kinetic limitations.

Conclusions

In summary, our work stands out as developing one of the highest-capacity polyanionic cathodes. By a targeted substitution strategy, we have achieved almost full theoretical capacity, enhanced rate capability, and reasonable capacity retention in the monoclinic LiMBO_3 system. The improved Li activities are understood in relation to triggering Mn and Fe redox elements, stabilizing the framework, and modifying the Li transport mechanism by partial substitution. Yet, the capacity loss at higher rate requires further improvement. Given that the rate-dependency of achievable capacity likely occurs above 3.7 V upon charging, which corresponds to the $\text{Mn}^{2+}/\text{Mn}^{3+}$ redox reaction, it will be important to understand the interaction between Mn^{2+} oxidation and poor Li^+ transport as has also been observed in other compounds such as LiMnPO_4 .^{52, 53} Reducing particle size further with innovative synthesis methods may lead to even better rate performance. Still, our new composition shows much progress towards obtaining a large reversible capacity in borates, suggesting that this partially substituted LiMnBO_3 -based cathode can combine high stability and high capacity. We consider that, although the current properties may not be satisfactory for commercialization yet, the scientific advance made in this study can guide the direction of future research that can lead to commercial attention to the borate compounds.

Acknowledgements

This work is funded in part by Robert Bosch GmbH, Umicore, the MRSEC Program of the National Science Foundation under award number DMR-0819762, and by the Assistant Secretary for Energy Efficiency and Renewable Energy, Office of Vehicle

Technologies of the U.S. Department of Energy (DOE) under Contract No. DE-AC02-05CH11231, under the Batteries for Advanced Transportation Technologies (BATT) Program. This work has used the resources of The Materials Project supported by Basic Energy Sciences program of DOE under Grant No. EDCBEE, DOE Contract DE-AC02-05CH11231.

References

- J. Y. Wang, N. L. Yang, H. J. Tang, Z. H. Dong, Q. Jin, M. Yang, D. Kisailus, H. J. Zhao, Z. Y. Tang and D. Wang, *Angew. Chem. Int. Edit.*, 2013, **52**, 6417-6420.
- H. Ren, R. B. Yu, J. Y. Wang, Q. Jin, M. Yang, D. Mao, D. Kisailus, H. J. Zhao and D. Wang, *Nano Lett.*, 2014, **14**, 6679-6684.
- S. M. Xu, C. M. Hessel, H. Ren, R. B. Yu, Q. Jin, M. Yang, H. J. Zhao and D. Wang, *Energy Environ. Sci.*, 2014, **7**, 632-637.
- J. B. Goodenough and K. S. Park, *J. Am. Chem. Soc.*, 2013, **135**, 1167-1176.
- V. Etacheri, R. Marom, R. Elazari, G. Salitra and D. Aurbach, *Energy Environ. Sci.*, 2011, **4**, 3243-3262.
- G. Hautier, A. Jain, T. Mueller, C. Moore, S. P. Ong and G. Ceder, *Chem. Mater.*, 2013, **25**, 2064-2074.
- G. Ceder, *MRS Bull.*, 2010, **35**, 693-701.
- L. X. Yuan, Z. H. Wang, W. X. Zhang, X. L. Hu, J. T. Chen, Y. H. Huang and J. B. Goodenough, *Energy Environ. Sci.*, 2011, **4**, 269-284.
- A. Yamada, N. Iwane, Y. Harada, S. Nishimura, Y. Koyama and I. Tanaka, *Adv. Mater.*, 2010, **22**, 3583-3587.
- V. Legagneur, Y. An, A. Mosbah, R. Portal, A. L. La Salle, A. Verbaere, D. Guyomard and Y. Piffard, *Solid State Ionics*, 2001, **139**, 37-46.
- J. C. Kim, C. J. Moore, B. Kang, G. Hautier, A. Jain and G. Ceder, *J. Electrochem. Soc.*, 2011, **158**, A309-A315.
- K. J. Lee, L. S. Kang, S. Uhm, J. S. Yoon, D. W. Kim and H. S. Hong, *Curr. Appl. Phys.*, 2013, **13**, 1440-1443.
- Y. S. Lee and H. Lee, *J. Ceram. Process. Res.*, 2012, **13**, S237-S240.
- S. L. Li, L. Q. Xu, G. D. Li, M. Wang and Y. J. Zhai, *J. Power Sources*, 2013, **236**, 54-60.
- S. Afyon, D. Kundu, F. Krumeich and R. Nesper, *J. Power Sources*, 2013, **224**, 145-151.
- S. Afyon, D. Kundu, A. J. Darbandi, H. Hahn, F. Krumeich and R. Nesper, *J. Mater. Chem. A*, 2014, **2**, 18946-18951.
- R. Norrestam, *Z. Kristallogr.*, 1989, **187**, 103-110.
- H. Yamane, T. Kawano, K. Fukuda, T. Suehiro and T. Sato, *J. Alloy. Compd.*, 2012, **512**, 223-229.
- A. Yamada, N. Iwane, S. Nishimura, Y. Koyama and I. Tanaka, *J. Mater. Chem.*, 2011, **21**, 10690-10696.
- B. Kang and G. Ceder, *Nature*, 2009, **458**, 190-193.
- B. Kang and G. Ceder, *J. Electrochem. Soc.*, 2010, **157**, A808-A811.
- R. Dominko, M. Bele, M. Gaberscek, A. Meden, M. Remskar and J. Jamnik, *Electrochem. Commun.*, 2006, **8**, 217-222.
- A. Kokalj, R. Dominko, G. Mali, A. Meden, M. Gaberscek and J. Jamnik, *Chem. Mater.*, 2007, **19**, 3633-3640.
- S. K. Martha, J. Grinblat, O. Haik, E. Zinigrad, T. Drezen, J. H. Miners, I. Exnar, A. Kay, B. Markovsky and D. Aurbach, *Angew. Chem. Int. Edit.*, 2009, **48**, 8559-8563.
- I. Matts, H. L. Chen and G. Ceder, *ECS Electrochem. Lett.*, 2013, **2**, A81-A83.
- Z. L. Gong and Y. Yang, *Energy Environ. Sci.*, 2011, **4**, 3223-3242.
- J. C. Kim, X. Li, C. J. Moore, S. H. Bo, P. G. Khalifah, C. P. Grey and G. Ceder, *Chem. Mater.*, 2014, **26**, 4200-4206.
- D. H. Seo, Y. U. Park, S. W. Kim, I. Park, R. A. Shakoor and K. Kang, *Phys. Rev. B*, 2011, **83**.
- A. Gutierrez, N. A. Benedek and A. Manthiram, *Chem. Mater.*, 2013, **25**, 4010-4016.
- L. Wang, T. Maxisch and G. Ceder, *Phys. Rev. B*, 2006, **73**, 195107.
- G. Kresse and J. Furthmuller, *Phys. Rev. B*, 1996, **54**, 11169-11186.
- G. Kresse and D. Joubert, *Phys. Rev. B*, 1999, **59**, 1758-1775.
- G. Bergerhoff, R. Hundt, R. Sievers and I. D. Brown, *J. Chem. Inf. Comp. Sci.*, 1983, **23**, 66-69.
- O. S. Bondareva, M. A. Simonov, Y. K. Egorovtismenko and N. V. Belov, *Sov. Phys. Crystallogr.*, 1978, **23**, 269-271.
- G. L. W. Hart and R. W. Forcade, *Phys. Rev. B*, 2008, **77**, 224115.
- A. Y. Toukmaji and J. A. Board, *Comp. Phys. Commun.*, 1996, **95**, 73-92.
- G. Hautier, C. C. Fischer, A. Jain, T. Mueller and G. Ceder, *Chem. Mater.*, 2010, **22**, 3762-3767.
- G. Mills, H. Jonsson and G. K. Schenter, *Surf. Sci.*, 1995, **324**, 305-337.
- C. A. Schneider, W. S. Rasband and K. W. Eliceiri, *Nat. Methods*, 2012, **9**, 671-675.
- S. P. Ong, L. Wang, B. Kang and G. Ceder, *Chem. Mater.*, 2008, **20**, 1798-1807.
- L. Tao, G. Rousse, J. N. Chotard, L. Dupont, S. Bruyere, D. Hanzel, G. Mali, R. Dominko, S. Levasseur and C. Masquelier, *J. Mater. Chem. A*, 2014, **2**, 2060-2070.
- R. Malik, D. Burch, M. Bazant and G. Ceder, *Nano Lett.*, 2010, **10**, 4123-4127.
- R. D. Shannon, *Acta Crystallogr. A*, 1976, **32**, 751-767.
- S. H. Bo, K. W. Nam, O. J. Borkiewicz, Y. Y. Hu, X. Q. Yang, P. J. Chupas, K. W. Chapman, L. Wu, L. Zhang, F. Wang, C. P. Grey and P. G. Khalifah, *Inorg. Chem.*, 2014, **53**, 6585-6595.
- S. H. Bo, F. Wang, Y. Janssen, D. L. Zeng, K. W. Nam, W. Q. Xu, L. S. Du, J. Graetz, X. Q. Yang, Y. M. Zhu, J. B. Parise, C. P. Grey and P. G. Khalifah, *J. Mater. Chem.*, 2012, **22**, 8799-8809.
- J. C. Kim, D.-H. Seo and G. Ceder, *Adv. Energy Mater.*, 2015, **5**, 1401916.
- J. Lee, A. Urban, X. Li, D. Su, G. Hautier and G. Ceder, *Science*, 2014, **343**, 519-522.
- C. Delmas, H. Cognacouradou, J. M. Cocciantelli, M. Menetrier and J. P. Doumerc, *Solid State Ionics*, 1994, **69**, 257-264.
- S. H. Bo, G. M. Veith, M. R. Saccomanno, H. F. Huang, P. V. Burmistrova, A. C. Malingowski, R. L. Sacci, K. R. Kittilstved, C. P. Grey and P. G. Khalifah, *ACS Appl. Mater. Inter.*, 2014, **6**, 10840-10848.
- S. Afyon, C. Mensing, F. Krumeich and R. Nesper, *Solid State Ionics*, 2014, **256**, 103-108.
- Y. Yamashita, P. Barpanda, Y. Yamada and A. Yamada, *ECS Electrochem. Lett.*, 2013, **2**, A75-A77.
- H. Gwon, D. H. Seo, S. W. Kim, J. Kim and K. Kang, *Adv. Funct. Mater.*, 2009, **19**, 3285-3292.
- M. Yonemura, A. Yamada, Y. Takei, N. Sonoyama and R. Kanno, *J. Electrochem. Soc.*, 2004, **151**, A1352-A1356.

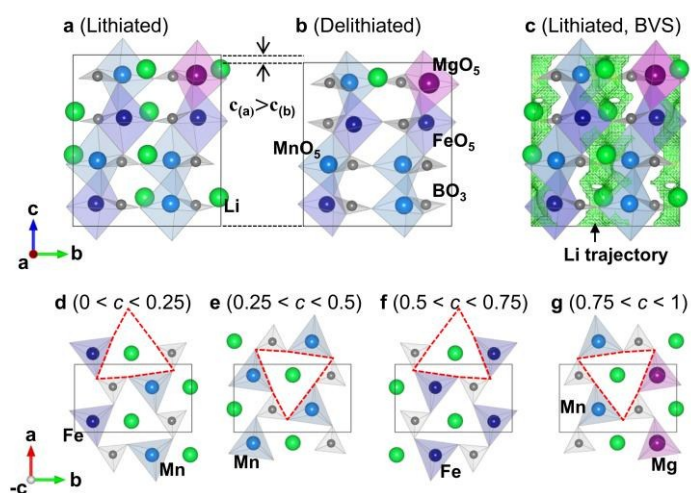


Figure 1. Predicted $\text{LiMn}_{0.5}\text{Fe}_{0.375}\text{Mg}_{0.125}\text{BO}_3$ unit cell. (a) Lithiated ($\text{Li} = 1$) and (b) delithiated ($\text{Li} = 0.125$) unit cells showing different c -lattice parameter (Green: Li, Blue: Mn, Navy: Fe, Purple: Mg, Grey: B in oxygen polyhedra). (c) Li trajectory visualized by a bond valence sum (BVS) method in the lithiated state. (d-g) Local arrangement of Mn, Fe, and Mg around Li at different positions along the c -axis. Red triangles form the 1-D migration channel along c -axis.

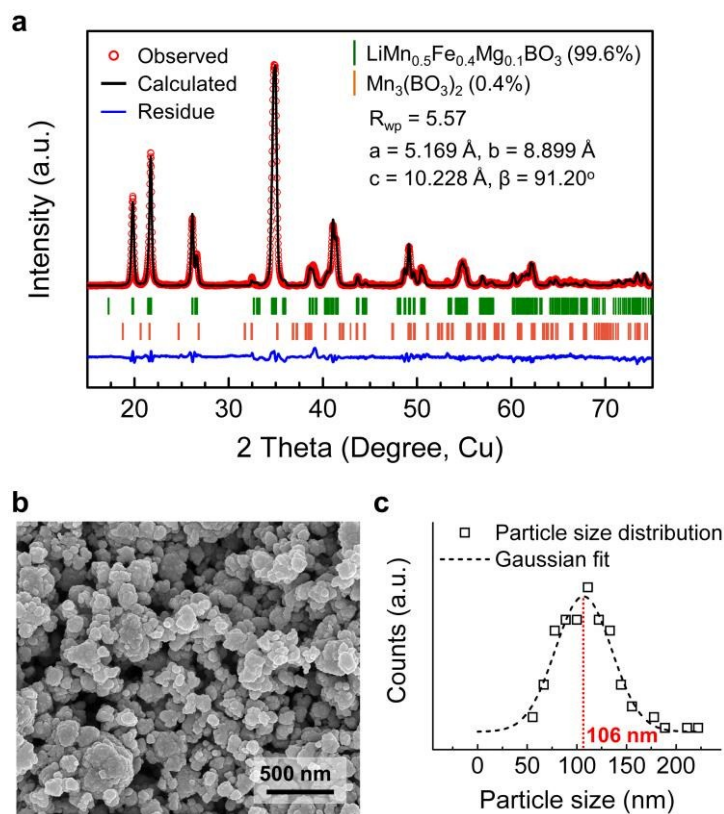


Figure 2. Monoclinic structure and particle morphology. (a) Profile matching of the XRD pattern by Rietveld refinement, (b) SEM image and (c) particle size distribution obtained from $\text{LiMn}_{0.5}\text{Fe}_{0.4}\text{Mg}_{0.1}\text{BO}_3$.

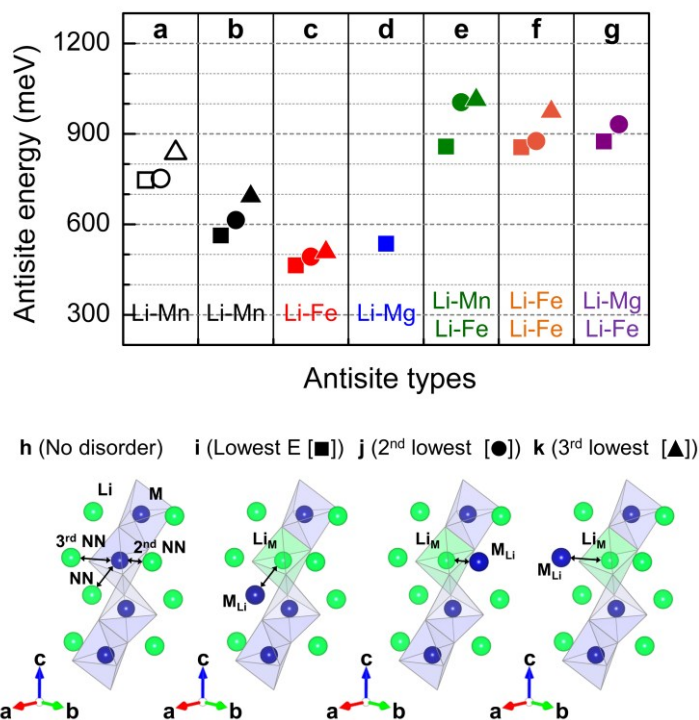


Figure 3. Antisite formation energies. (a) Li – Mn antisite formation energy in unsubstituted LiMnBO_3 and (b-g) antisite formation energies in $\text{LiMn}_{0.5}\text{Fe}_{0.375}\text{Mg}_{0.125}\text{BO}_3$ with respect to antisite types: (b) Li – Mn, (c) Li – Fe, and (d) Li – Mg at 1/16 concentration, and (e) Li – Mn, (f) Li – Fe, and (g) Li – Mg at 1/16 concentration on top of the 1/16 lowest energy Li – Fe configuration. (h-k) Geometrical configurations of antisite pairs. The nearest neighbor (Li) is denoted as NN.

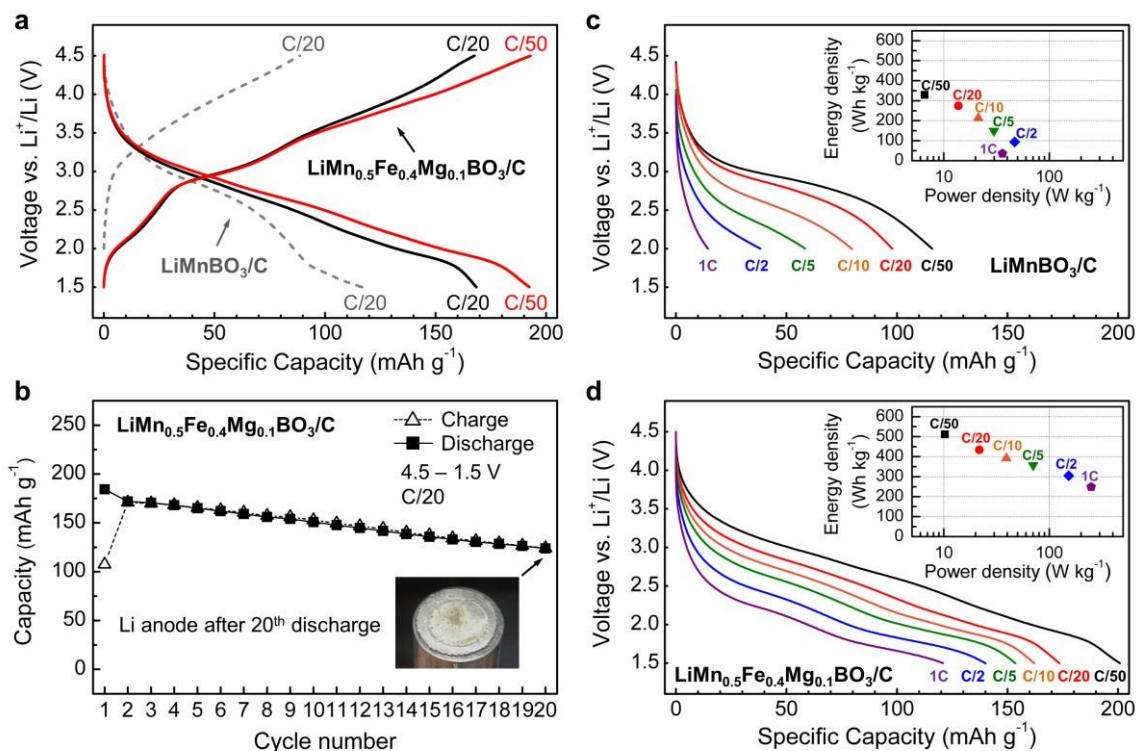


Figure 4. Electrochemical performance. (a) Representative (second) charge and discharge curves for $\text{LiMn}_{0.5}\text{Fe}_{0.4}\text{Mg}_{0.1}\text{BO}_3/\text{C}$ at C/50 and C/20 rates (RT), and for LiMnBO_3/C at C/20 (RT) and (b) capacity retention of $\text{LiMn}_{0.5}\text{Fe}_{0.4}\text{Mg}_{0.1}\text{BO}_3/\text{C}$ cycled at a C/20 rate (RT). Discharge capacities of (c) LiMnBO_3/C and (d) $\text{LiMn}_{0.5}\text{Fe}_{0.4}\text{Mg}_{0.1}\text{BO}_3/\text{C}$ at RT achieved at designated rates. The cell was charged at C/50, held at 4.5 V for 2 h, and then discharged at designated rates ranging from C/50 to 1C.

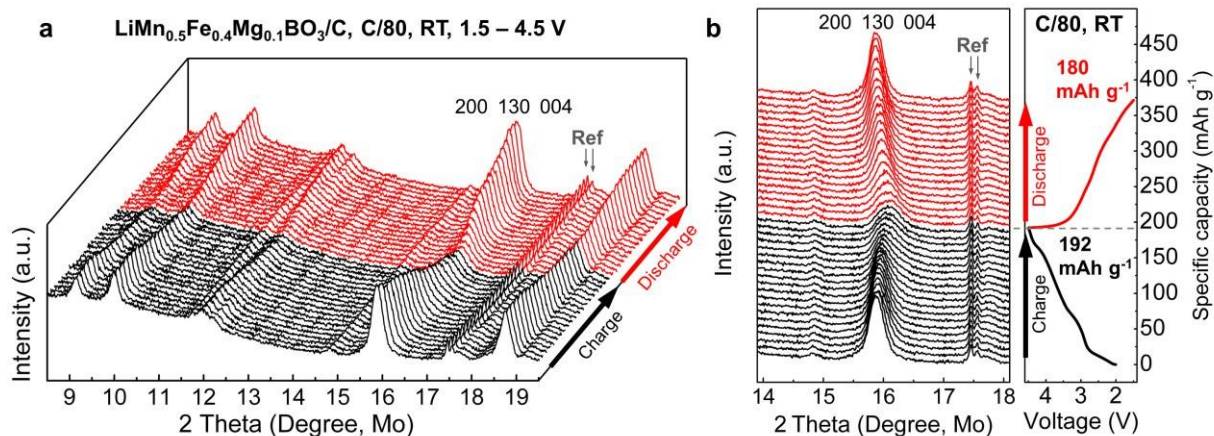


Figure 5. *In situ* XRD. *In situ* XRD patterns of $\text{LiMn}_{0.5}\text{Fe}_{0.4}\text{Mg}_{0.1}\text{BO}_3/\text{C}$ during charging and discharging at a C/80 rate. (a) 20 whole patterns with 5% resolution in Li contents for charging and 19 patterns for discharging (39 individual patterns), (b) diffraction around a lumped peak of (200), (130), and (004) and the corresponding voltage profile

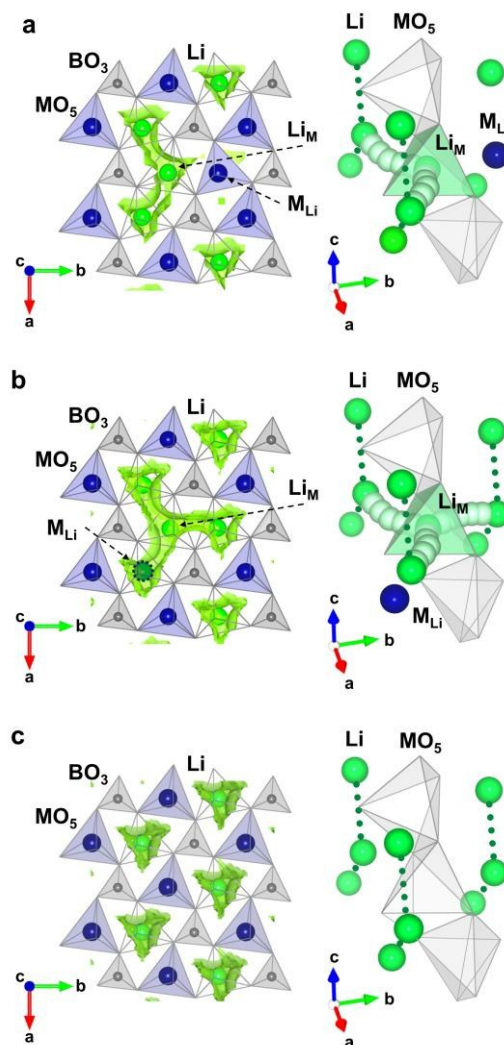


Figure 6. Local Li trajectories in various $\text{Li}_M - \text{M}_{\text{Li}}$ ($M = \text{Mn, Fe, Mg}$) antisite configurations in $\text{LiMn}_{0.5}\text{Fe}_{0.375}\text{Mg}_{0.125}\text{BO}_3$. (a) The second lowest energy (Li-trapping), (b) the lowest energy antisite (Li-redirecting), and (c) antisite-free configurations (1-D Li). In each case, the Li channel direction is along the c -axis, so the figure shows whether there is cross-channel diffusion.

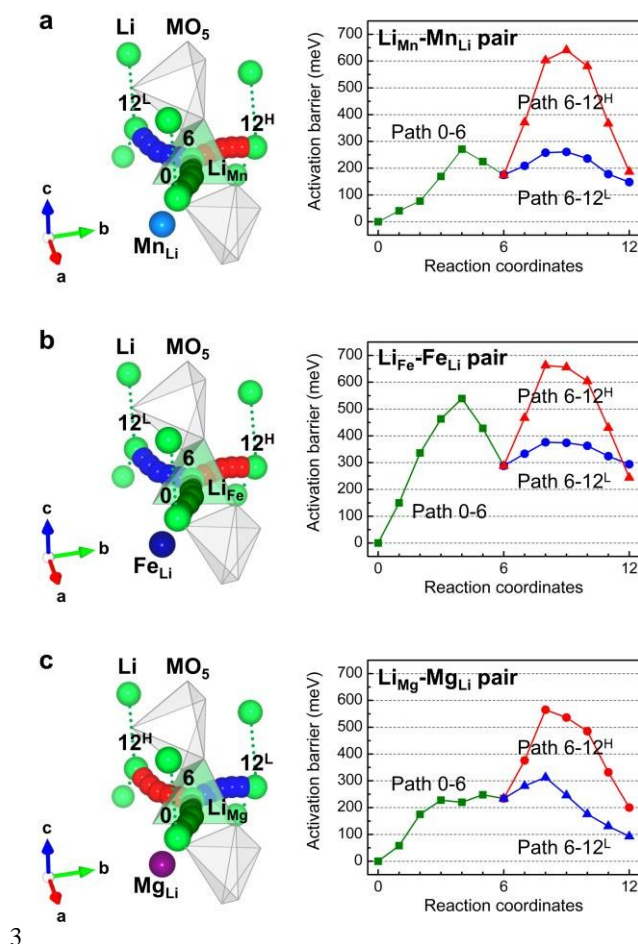


Figure 7. Local Li trajectories around the lowest energy $\text{Li}_{\text{M}}-\text{M}_{\text{Li}}$ configurations and associated activation barriers for crossover. M = (a) Mn, (b) Fe, and (c) Mg.

Broader context

Li intercalation materials framed with polyanion groups can offer high stability against oxygen loss, thereby enhancing safety over common oxide cathode materials. However, the specific capacity of most polyanionic cathodes is limited due to the large formula weight of the polyanions. A simple borate (BO_3) is the lightest possible polyanion group with low mass to negative charge ratio. As a result, lithium transition metal borates can have both high theoretical capacity and high operating safety. However, despite these promising motivations, borates remain relatively unexplored as a cathode material for lithium ion batteries. In this work, we develop a new composition within the borate framework that achieves a near theoretical capacity, improved rate capability, and reasonable capacity retention. We believe that the superior electrochemical properties demonstrated in this study will bring more attention to the borate chemistry as a potential alternative to current Li-ion battery cathodes.